

ARTICLE

Open Access

Conformal bumped electrode web for chronic ECoG recordings in swine

Minghao Wang^{1,2}, Hao Jiang¹, Chuner Ni¹, Xinhua Zhou¹, Yuchen Xu³, Siyan Shang¹, Xiaoli You⁴, Wenhao Wang¹, Chaojie Zhou¹, Wenbin Zhang¹, Xinyi Wang¹✉, Shaomin Zhang⁵✉, Lufeng Shi⁶ and Bowen Ji⁴✉

Abstract

The acquisition of high-quality electrocorticogram (ECoG) signal is of great significance for the diagnosis and treatment of neurological diseases such as high amputation, visual injury, epilepsy and Parkinson's disease. Currently, flexible ECoG electrodes have received attention due to their low mechanical mismatch and minimally invasive characteristics. However, the traditional ECoG electrodes are non-stretchable planar structures that cannot be conformal with the cerebral cortex, which is in constant motion and has sulci and gyri structure. In this work, a flexible stretchable ECoG electrode with bumped electrodes was developed to alleviate these problems. Firstly, the mechanical simulation results show that this stretchable electrode structure can effectively reduce the stress mismatch between electrode and tissue interface. Secondly, the results of cyclic voltammetry scanning and mechanical tensile experiments show that the stretchable ECoG electrode structure can be conformally attached to the surface of the cerebral cortex and maintain good electrochemical stability during continuous stretching. Third, the bumped electrode has a larger adhesive force than the planar electrode and can significantly reduce the background noise by conformal attachment and electrochemical modification of PEDOT:PSS. Most importantly, in vivo animal experiments showed that the stretchable ECoG electrode can continuously record high-quality ECoG signals on the surface of the cerebral cortex of swine over an area of $22 \times 22 \text{ mm}^2$ for more than 5 weeks.

Introduction

Implantable neural electrodes must be flexible enough to meet the requirements of conformal attachment to the brain surface and internal tissue deformation. In particular, the electrocorticogram (ECoG) electrode has experienced a development process from rigidity to flexibility, and the soft ECoG electrode has become an important development trend in the future. Normann et al. at the University of Utah proposed the Utah electrode Array in 1997, a rigid ECoG electrode that allows the electrode to penetrate neural tissue, thus recording broader and deeper neuronal activity^{1,2}. However, the

Young's modulus of Utah electrode is significantly different from that of brain tissue, which is easy to cause serious foreign body reaction and neuronal necrosis³.

In recent years, flexible polymer materials such as polyimide (PI)⁴, polyethylene terephthalate (PET)⁵ or parylene⁶ with good micro-nano fabrication compatibility have been widely used to manufacture neural electrodes with Young's modulus of about 2 to 4 GPa. In 2022, S. A. Dayeh's team⁷ proposed a high-throughput ECoG microelectrode with 1024 channels, which greatly improved the coverage area and spatial resolution on the cortical surface. In 2025, P. Konrad conducted the first preliminary intraoperative acute experiment of cortical electrical imaging mapping in a human study, using a novel thin-film ECoG array containing 1024 microelectrodes⁸. To realize the stretchability of the flexible materials, it is a feasible strategy to fabricate non-stretchable flexible materials into curved wire structures to realize the stretchability^{9–14} as summarized in Table 1. In 2023, Jia Liu's group introduced a method to precisely implant

Correspondence: Xinyi Wang (wxy317@hdu.edu.cn) or Shaomin Zhang (shaomin@zju.edu.cn) or Bowen Ji (bwji@nwpu.edu.cn)

¹MOE Engineering Research Center of Smart Microsensors and Microsystems, School of Electronics and Information, Hangzhou Dianzi University, Hangzhou, China

²Wenzhou Institute of Hangzhou Dianzi University, Wenzhou, China

Full list of author information is available at the end of the article

These authors contributed equally: Minghao Wang, Hao Jiang, Chuner Ni.

© The Author(s) 2026



Open Access This article is licensed under a Creative Commons Attribution-NonCommercial-NoDerivatives 4.0 International License, which permits any non-commercial use, sharing, distribution and reproduction in any medium or format, as long as you give appropriate credit to the original author(s) and the source, provide a link to the Creative Commons licence, and indicate if you modified the licensed material. You do not have permission under this licence to share adapted material derived from this article or parts of it. The images or other third party material in this article are included in the article's Creative Commons licence, unless indicated otherwise in a credit line to the material. If material is not included in the article's Creative Commons licence and your intended use is not permitted by statutory regulation or exceeds the permitted use, you will need to obtain permission directly from the copyright holder. To view a copy of this licence, visit <http://creativecommons.org/licenses/by-nc-nd/4.0/>.

Table 1 Performance Comparison to Other Stretchable Implantable Electrode Interface

Correlational research	Electrode structure	Stretchable structure	Electrode modification	Substrate	Animal species
Lee et al. ¹²	Flat	Wavy wires	Alginate/ PEDOT:PSS	PDMS/PI	Rat
Zhao et al. ¹⁵	Flat	Mesh structure	\	SU-8	Mouse
Ji et al. ¹⁶	Flat	Serpentine wires	PEDOT:PSS	Bacterial cellulose/ Parylene-C	Mouse
Kwon et al. ²⁹	Flat	\	PR:PEDOT	PDMS	Mouse/octopus
Qinai et al. ³⁰	Microneedle	Serpentine wires	Pt-black	PI	Aplysia californica
[This work]	Bumped	Serpentine wires and substrate	PEDOT:PSS	Parylene-C	Pig

electronics with an open, unfolded mesh structure across multiple brain regions in the mouse¹⁵. The open mesh structure forms a stable interwoven structure with the neural network, preventing probe drifting and showing no immune response and neuron loss during the year-long implantation. Bowen Ji's group proposed a micro-ECoG electrode named "Brainmask", which comprises a bacterial cellulose film as the substrate and separated stretchable parylene-C microelectrodes bonded on the top surface¹⁶. Brainmask can not only guarantee the precise position of microelectrode sites attached to any nonplanar epidural surface but also improve the long-lasting signal quality during in vivo recording, validated for one week. Table. 1

The use of intrinsically stretchable materials such as polydimethylsiloxane (PDMS) as neural electrode substrates, with a Young's modulus of about 1 kPa to 1 MPa, can significantly reduce the mechanical mismatch of neural tissue^{17–25}. In 2019, M. Nishizawa introduced a fully compliant organic subdural electrode fabricated by embedding an array of PEDOT-modified carbon fibers (PEDOT-CF) into a polyvinyl alcohol (PVA) hydrogel matrix²⁶. The stretchable, reticular structure of PEDOT-CF enables stable integration with the PVA hydrogel, while the hydrogel matrix itself minimizes contact impedance with the brain surface—critical for high-fidelity signal acquisition. In 2022, Zhenan Bao's team²⁷ developed a flexible stretchable (100%) microelectrode array based on PDMS and Poly(3,4-ethylenedioxythiophene):poly (styrenesulfonate) (PEDOT:PSS) carbon-based electrode materials to collect stable EMG signals and achieve local neuroregulation. In 2024, Momin's team introduced a 3D-printable flexible and stretchable porous (FSP) neural probe²⁸. Due to its porous structure and the materials used in its fabrication (PEDOT, PDMS), the FSP neural probe can be manually stretched up to 100% without breaking. However, the processing accuracy of stretchable PDMS neural electrodes is not enough for high-density ECoG electrode. In

addition, the planar electrode structure is difficult to form close contact with the non-planar cortical surface.

In the past decade, flexible bumped microelectrodes have been developed because they can conform to deforming tissues, thereby facilitating targeted recording of the neurons. In 2014, Wen Li's group developed a droplet backside exposure (DBE) method to fabricate flexible optrodes, which have a raised microneedle electrode structure that can be inserted into the cortex to achieve close contact like the Utah electrode²⁹. In 2024, Zhao's group used a unique hybrid fabrication scheme based on laser micromachining and transfer printing to fabricate stretchable (60% to 90%) microneedle electrode arrays for sensing local intramuscular electromyography signals ex vivo³⁰. However, these ECoG electrodes with bumped electrode points do not possess the stretching property, and their tissue compatibility needs to be improved.

In this work, a flexible stretchable ECoG electrode with bumped electrodes was developed for high conformal neural recording. PEDOT is modified on the bumped electrodes to reduce interface impedance and improve biocompatibility. In-vitro simulated neural recording experiments have shown that the electrochemically modified bumped electrodes can enhance the recording performance of the electrode by reducing the interface impedance and achieving conformal adhesion. Moreover, the ability of the electrodes to steadily record high-quality ECoG signals was demonstrated through chronic implantation experiments in swine's brain.

Results

Design and fabrication

The schematic diagram of the ECoG electrode is shown in Fig. 1a, featuring bumped electrode sites and serpentine stretchable wires. The conductive pads were connected to a FPC cable by hot-press bonding with Anisotropic Conductive Film (ACF) adhesive³¹. A total of 64 electrode sites (0.9 mm in diameter) are evenly spaced on the

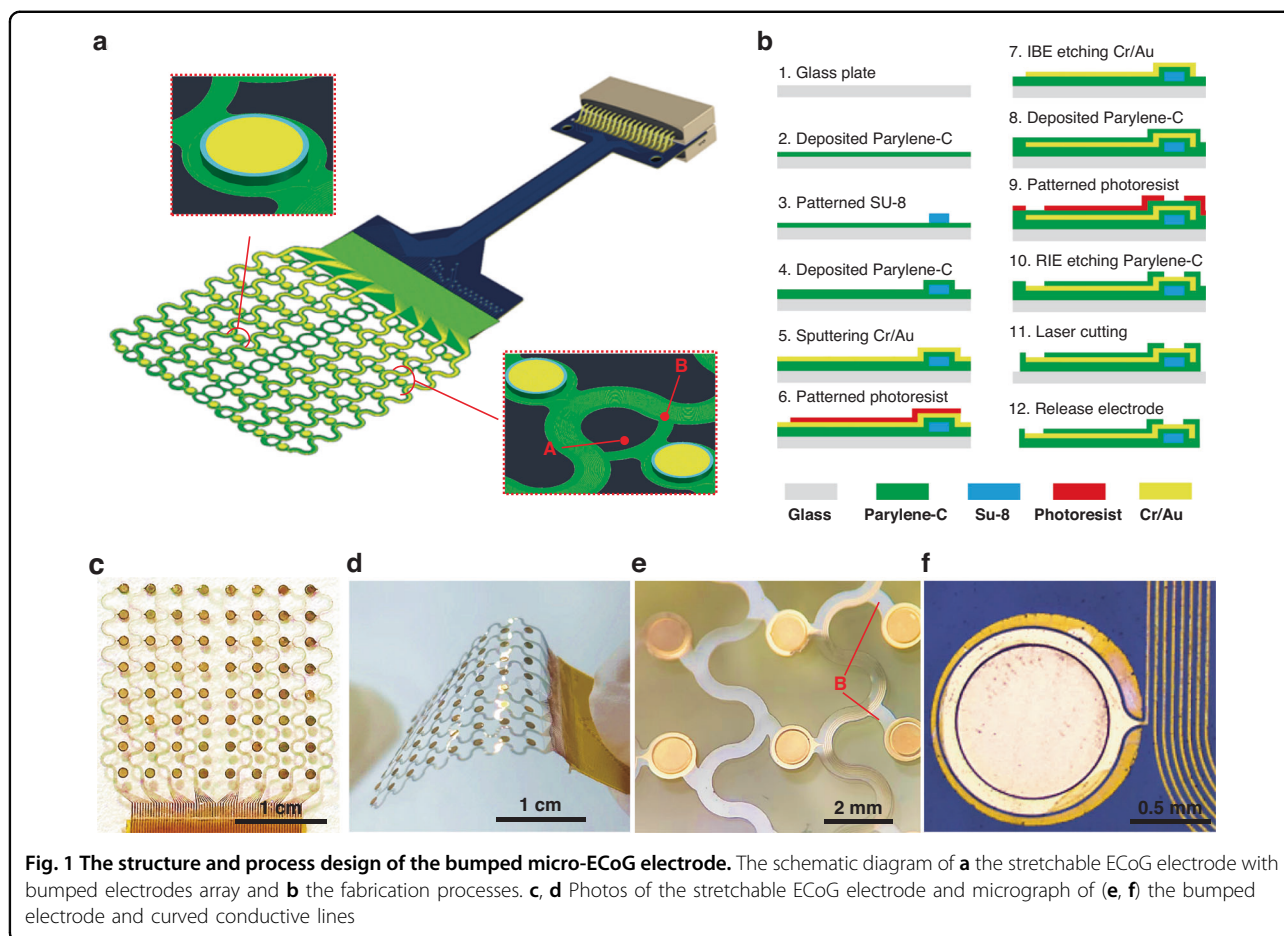
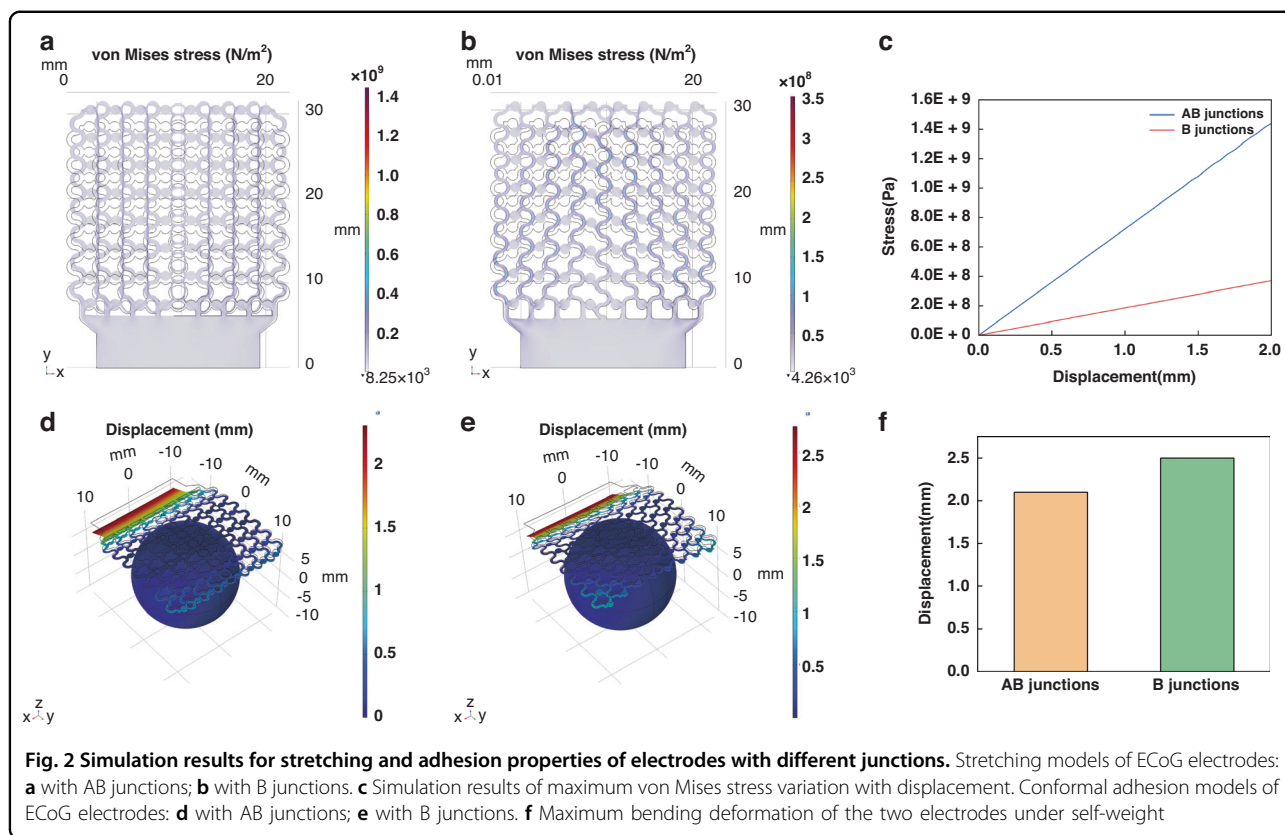


Fig. 1 The structure and process design of the bumped micro-ECoG electrode. The schematic diagram of **a** the stretchable ECoG electrode with bumped electrodes array and **b** the fabrication processes. **c**, **d** Photos of the stretchable ECoG electrode and micrograph of **(e, f)** the bumped electrode and curved conductive lines

stretchable substrate, with adjacent spacing of 3 mm. To prevent the electrode sites from deforming and shifting during the stretching process, two connection junctions (A and B) as shown in the inset of Fig. 1a were designed. The schematic diagram of fabrication process for the ECoG electrode is shown in Fig. 1b. First, a glass wafer was prepared and cleaned with anhydrous ethanol and deionized water. Then, a layer of 3 μm thick Parylene-C was deposited on the glass as the substrate. Subsequently, a layer of 30 μm thick SU-8 2015 was spin-coated onto the Parylene-C and patterned by photolithography to fabricate the bumped structure. After that, another layer of 5 μm thick Parylene-C was deposited as the bottom insulation layer. Next, 20 nm of Cr and 200 nm of Au were sputtered and patterned to form the electrode sites, conductive wires and metal pads. To avoid thinning or breaking of the wires near the bumped electrode sites due to overexposure to the photoresist, the mask pattern at the junction of wire and electrode site is widened as shown in the inset of Fig. 1a. After that, another 5 μm thick of Parylene-C layer was deposited as the top insulation layer, and conductive windows were patterned by photoresist. Finally, reactive ion etching was used to etch

the Parylene-C and expose the electrode sites and metal pads. The ECoG electrodes were released from the glass wafer by laser cutting. The Parylene-C substrate and insulation layers were also patterned in this step to form the serpentine structure as shown in Fig. 1(c, d). The bumped electrodes with only junction B to the serpentine wires were shown in Fig. 1e. It is evident that without junction A, the electrodes can still maintain a fixed position without warping. Figure 1f presents a micrograph of a single bumped electrode, which reveals that the diameter of the exposed electrode, the bumped structure, and the electrode metal layer increase progressively. In addition, the connecting wire between the serpentine line and the bumped electrode site is designed into a 'horn shape', with the part close to the electrode gradually widening. These redundant size designs ensure the metal layer remains continuous at the steps of the bumped structure, thereby preventing interruptions in signal transmission. The non-stretchable and stretchable planar ECoG electrode without bumped structures are fabricated with the similar processes. Specifically, the process for the stretchable planar electrode only requires the removal of the SU8 patterning steps, while the process for the



non-stretchable planar electrode also needs the removal of the serpentine line laser cutting step.

Stress and strain simulation analysis

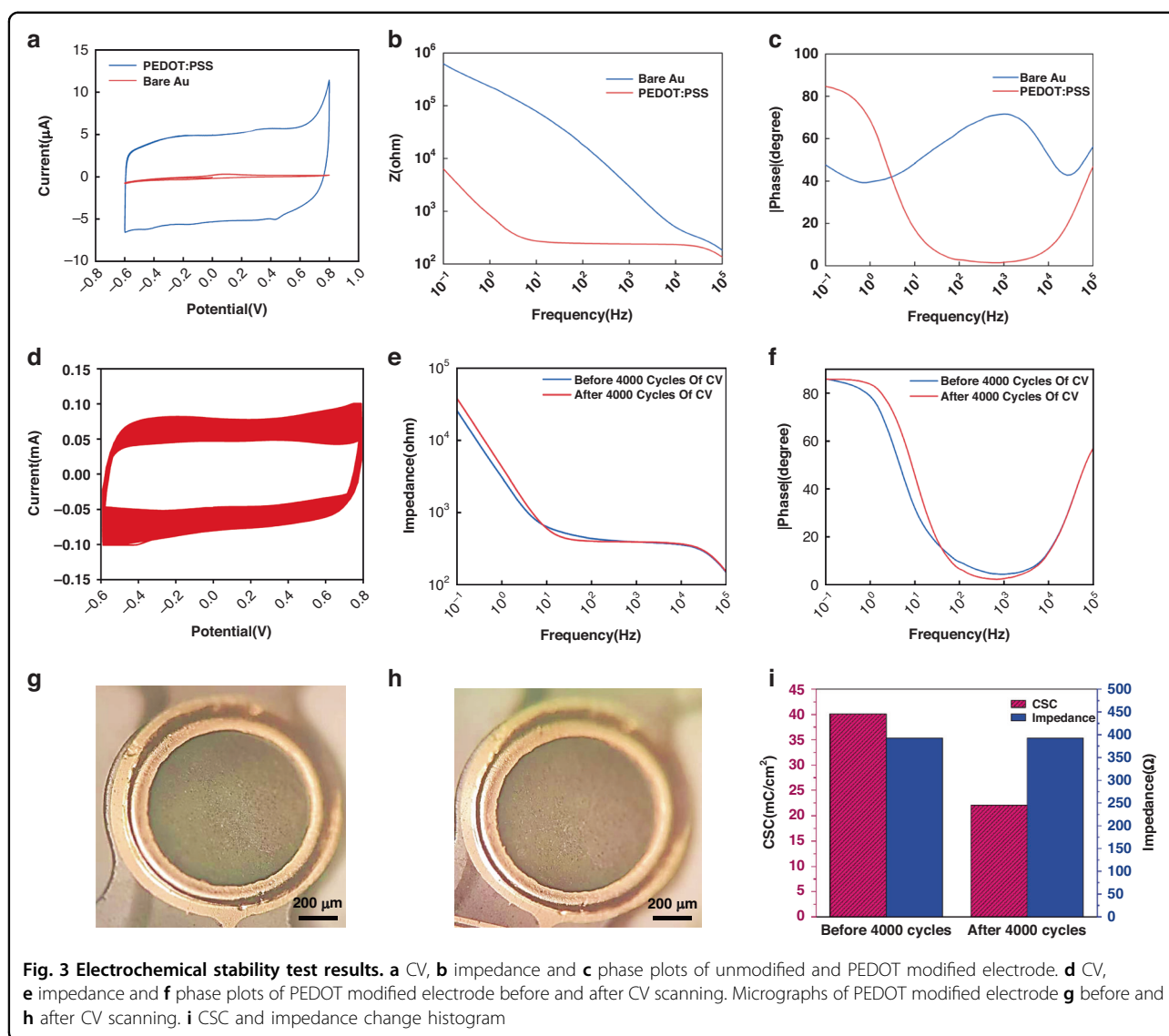
First, the bending stiffness and stretchability of the ECoG electrodes were simulated and analyzed via finite element analysis (FEA), with direct comparisons conducted against electrodes featuring AB junctions (Fig. 2a) and a B junction (Fig. 2b). As illustrated in Fig. 2c, the maximum stress of the ECoG electrode with the B junction during the entire stretching process is significantly lower than that of the electrode with AB junctions—indicating superior stretchability. For the evaluation of bending stiffness, both the AB-junction electrode and B-junction electrode were attached to a 5 cm-diameter brain model. As shown in Fig. 2(d–f), the ECoG electrode with the B junction is more compliant to deformation under its own weight and can conformally adhere to the spherical model. These simulation results demonstrate that, compared with ECoG electrodes with AB junctions, those with a B junction exhibit greater susceptibility to both stretching and bending deformation. Such characteristics enable them to conform more effectively to the surface of brain tissue, thereby improving the stability of signal acquisition. However, this asymmetric structure will exhibit tilting during large stretching, and the greater

the tensile strain, the more severe the tilting. Nevertheless, considering that the actual tensile strain of brain tissue will not exceed 10%, the single-node design was still opted to ensure the conformal adhesion capability of the electrodes under small tensile strains.

Electrochemical stability characterization

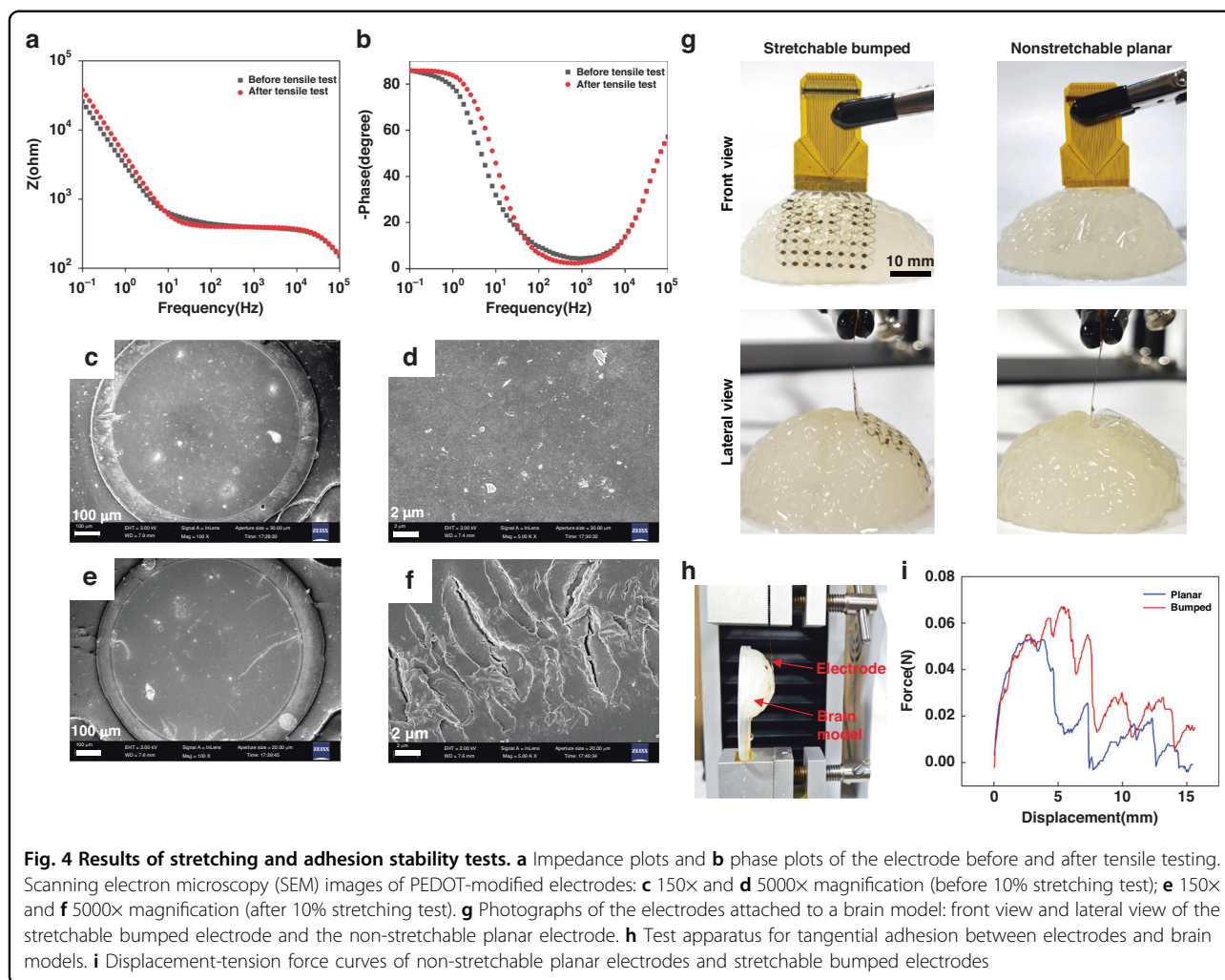
To investigate the electrochemical performance of the electrodes, CV curves, EIS curves, and CV scanning durability tests were conducted for the electrodes before and after modification. As presented in Fig. 3(a–c), after modification with PEDOT, the charge storage capacity (CSC) of the electrode increased dramatically from 0.48 mC/cm² to 40.11 mC/cm²—this enhancement is attributed to PEDOT's high double-layer capacitance and pseudocapacitance characteristics. Concurrently, the electrode impedance decreased significantly across the entire frequency range post-modification. Specifically, at 1 kHz, the impedance dropped from 2.42 ± 0.72 kΩ to 0.32 ± 0.08 kΩ, while the phase delay reduced from -70.23 ± 2.89° to -3.70 ± 1.80°.

As shown in Fig. 3(d–f), after 4,000 cycles of CV scanning (potential range: -0.6 V to 0.8 V; scan rate: 1 V/s), the CSC of the PEDOT-modified electrode decreased from 40.11 mC/cm² to 22.06 mC/cm². This is because the repeated oxidation-reduction during CV cycles damages



PEDOT's conjugated structure or the integrity of molecular chains, directly leading to the loss of active sites. In Fig. 3(e, f), except for slight attenuation of electrochemical performance was observed in the low-frequency range (0.1–10 Hz) after scanning, the impedance and phase remained nearly unchanged in the primary frequency domain (10 Hz–1 kHz) of the ECoG signals. The changes in CSC and impedance are mainly affected by the pseudocapacitance and double-layer capacitance of PEDOT. From the perspective of impedance spectroscopy, the slight reduction in impedance at medium and high frequencies is mainly attributed to the increase in double-layer capacitance. This indicates that CV scanning induces the formation of numerous micro-pores in PEDOT during repeated contraction and expansion processes, which increases its effective surface area and thereby enhances the double-layer capacitance. In contrast, the increase in

impedance at low frequencies is primarily caused by the decrease in pseudocapacitance. This suggests that CV scanning leads to the aging and detachment of part of the PEDOT structure, reducing the electrochemical activity of the electrode surface and thus decreasing the pseudocapacitance. Combined with the variation trend of CSC, it can be concluded that the decrease in pseudocapacitance is the main factor contributing to the reduction in CSC, indicating that CV scanning can induce the aging and structural detachment of PEDOT. Additionally, optical micrographs of the PEDOT-modified electrode before and after scanning (Fig. 3(g, h)) revealed no obvious material shedding, delamination, or cracking. By comparing the CSC and impedance data in Fig. 3(i), it can be concluded that the PEDOT-modified bumped electrode structure exhibits excellent electrochemical performance and long-term stability.



Tensile mechanical characterization

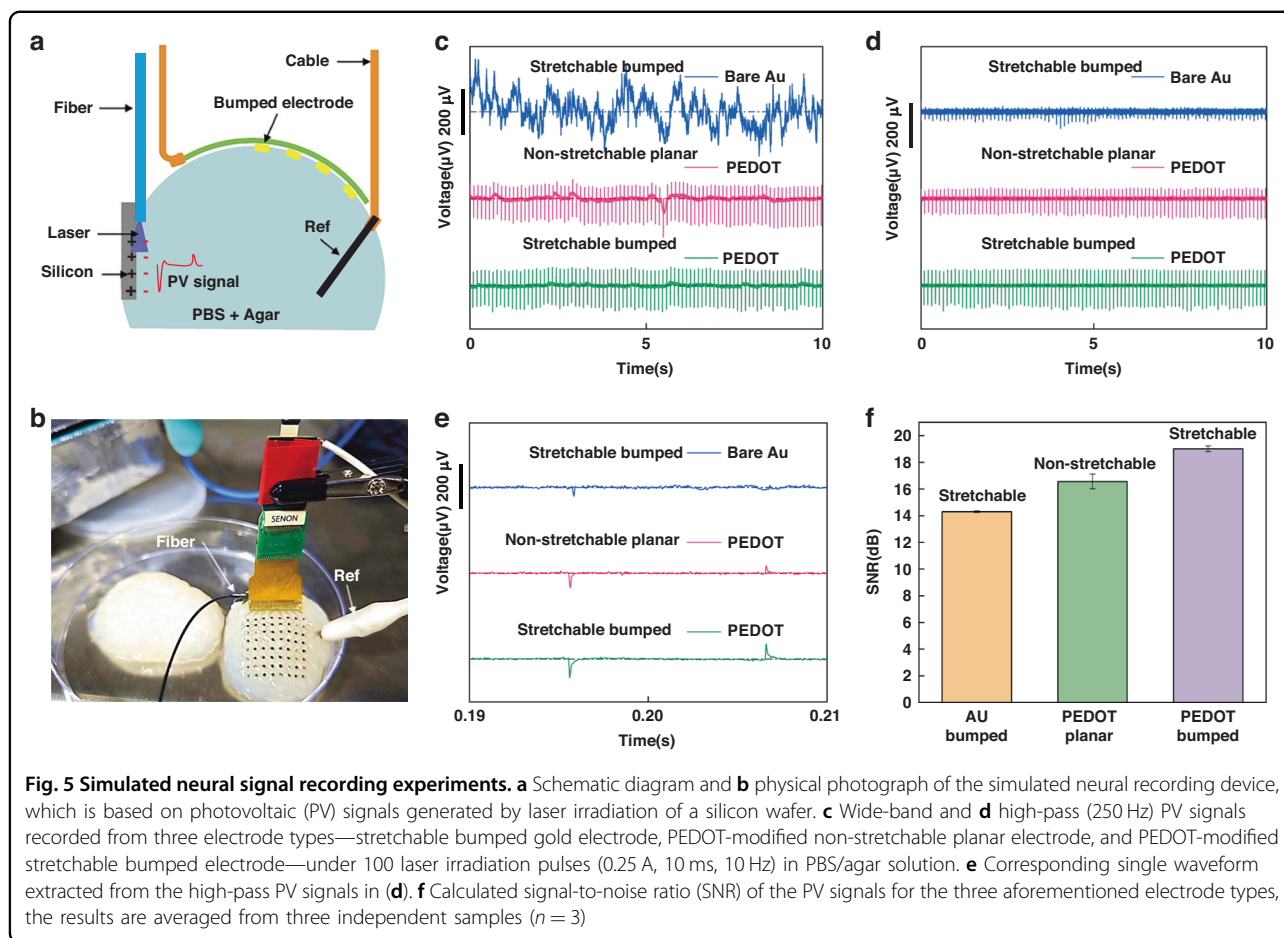
To assess the stretchability of the stretchable electrodes, they were subjected to 2500 cycles of cyclic tensile testing at 10% strain—this test aimed to evaluate their mechanical performance and durability under repeated deformation. As shown in Fig. 4a, after 2500 cycles of tensile testing, the electrode impedance at 1 kHz increased slightly from 239.4 Ω to 250 Ω , while the phase delay decreased marginally from -1.6° to -1.8° ; these changes correspond to only 4.4% and 12.5% variations, respectively. Such minimal fluctuations demonstrate the electrode's excellent stretchability and electrochemical stability.

The microscopic morphology of the electrode sites before and after stretching was further characterized, as presented in Fig. 4(c–f). Prior to the tensile test, poly(3,4-ethylenedioxythiophene) (PEDOT) uniformly covered the surface of the bumped electrode, with no surface cracks observed. At high magnification, PEDOT exhibited a granular microstructure—this morphology

explains the microscopic mechanism underlying its low interfacial impedance. After 2500 cycles of 10% stretching, a small number of nanoscale cracks appeared at the electrode edges; high-magnification images revealed that the width of these cracks was on the order of hundreds of nanometers. Overall, under 10% strain (a relatively large strain level), PEDOT only developed nanoscale cracks in a very limited area at the electrode edges. Notably, the strain naturally generated by brain tissue is typically far less than 10%. Thus, it can be concluded that PEDOT-modified electrodes can maintain mechanical stability for long-term implantation in brain tissue.

Adhesion mechanical characterization

To evaluate the conformality of the electrode with brain tissue, a comparative analysis was conducted between a stretchable bumped electrode and a non-stretchable planar electrode (of identical thickness and material), as presented in Fig. 4(g). From a frontal view,



the stretchable bumped electrode—featuring a serpentine structure—can conformally adhere to the surface of the irregular cerebral cortex. In contrast, the non-stretchable planar electrode exhibits noticeable wrinkles. From a side view, the stretchable electrode maintains tight adhesion to the cerebral cortex across its entire surface, whereas the edges of the planar electrode show significant warping and gaps. Regarding adhesion performance, as illustrated in Fig. 4(h, i), the stretchable electrode with a bumped structure requires a much higher tensile force (70 mN) to slide along the tangential plane of the brain model. These results demonstrate that, compared with the non-stretchable planar electrode, the stretchable bumped electrode offers two key structural advantages: superior conformal adhesion and reliable positioning.

Photovoltaic pulses simulated neural signal recording

In order to evaluate the influence of electrode impedance on the performance of neural signal recording, the PV signals and thermal noise shown in Fig. 5(a, b) were used to simulate the action potentials and background noise of neurons for bench testing. The theoretical

amplitude of thermal noise can be calculated using the Johnson-Nyquist Noise:

$$V = \sqrt{4k_B TRf}$$

where V denotes the theoretical root mean square (RMS) of the thermal noise voltage, k_B is the Boltzmann constant, T represents the temperature, f is the bandwidth for thermal noise measurement, and R stands for the device impedance. From this formula, it can be inferred that under identical conditions, the lower the electrode impedance, the smaller the background noise amplitude. Consequently, as illustrated in Fig. 5(c–f), the PEDOT:PSS-modified electrode exhibits lower background noise and a higher signal-to-noise ratio (SNR) across both high- and low-frequency ranges. After calculation by Matlab, the measured RMS signal and RMS noise amplitudes of the electrode before PEDOT:PSS modification are 73.66 μV and 2.77 μV , respectively, corresponding to an SNR of 14.25 dB; for the electrode after modification, the measured RMS signal and RMS noise amplitudes are 180.01 μV and 2.17 μV , with a corresponding SNR of 19.18 dB. It is evident that the variation

trend of the experimentally measured SNR and RMS noise data is consistent with the results predicted by the Johnson-Nyquist Noise formula.

Beyond the effect of the modified material, the adhesion state between the electrode and tissue also influences the quality of signal recording. Notably, certain channels of the sheet electrode showed severely degraded signal quality, which was attributed to poor contact with the brain model. As shown in Fig. 5f, the SNR of the PEDOT-modified stretchable electrode (19.18 dB) is higher than that of the PEDOT-modified sheet electrode (17.15 dB). All the above results demonstrate that the PEDOT:PSS-modified stretchable electrode exhibits the optimal performance in recording simulated neural signals. This superiority is primarily attributed to its lower interfacial impedance and stronger ability to achieve tight interface adhesion with tissue.

Acute neural signals recording

To verify the in vivo recording performance, the ECoG electrode was implanted onto the surface of the motor cortex of the mini pig's brain. The stretchable ECoG electrodes are indeed highly prone to folding due to electrostatic forces and intermolecular forces. To avoid this issue, the electrodes were immersed in an alcohol solution to unfold the electrodes. When transfer is required, a glass slide is inserted into the alcohol solution, allowing the stretchable electrode to come into contact with the glass slide in the solution. Subsequently, the glass slide was pulled out of the solution slowly, and the electrode can be smoothly adsorbed onto the surface of the glass slide. Before implantation, physiological saline can be dropped onto the surface of the glass slide to weaken the intermolecular forces between the electrode and the glass slide. Afterwards, the side of the glass slide with the adsorbed electrode is attached to the surface of the cerebral cortex, and then the glass slide is pulled away tangentially.

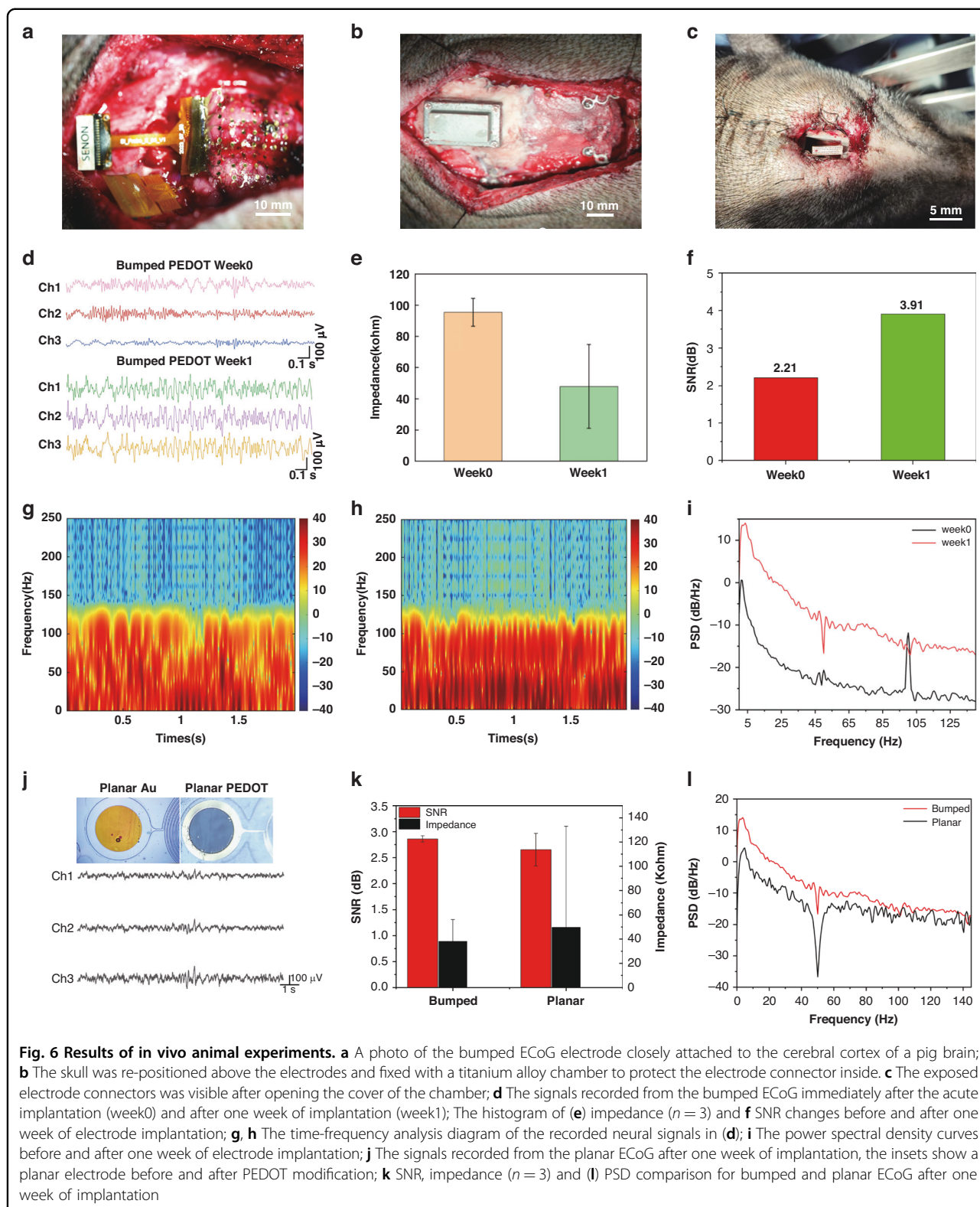
As shown in Fig. 6a, the stretchable electrode is closely attached to the surface of the cortex, and the bumped electrodes on the surface make it almost impossible to shift. In Fig. 6b, the electrode connector can be completely placed inside the titanium alloy chamber, thus avoiding mechanical damage. However, since the bottom of the chamber was not isolated from the skull tissue, this resulted in a small amount of blood accumulation inside the chamber one week after the implantation (Fig. 6c). It is precisely for this reason that some of the channels were short-circuited, preventing the recording of valid neural signals. By comparing the neural signals before and after one week of implantation (Fig. 6d), it can be seen that the amplitude of the ECoG signal has increased and the fluctuations have become more pronounced. At the same time, the impedance at the electrode and tissue interface also significantly decreased as depicted in Fig. 6e, which

might be due to the alleviation of edema and bleeding caused by the acute injury. Further analysis in Fig. 6f revealed that the SNR of the recorded neural signals increased from 2.21 in week0 to 3.91 in week1. The time-frequency analysis results of the neural signals in Fig. 6(g–i) show that the power of the neural signals within 0–150 Hz significantly increased after one week implantation, and the power spectral density also significantly improved throughout the entire low-frequency range. It can be inferred that the increase in signal amplitude and power is due to the reduction in the impedance of the neural interface and the increase in cell activity.

In Fig. 6(j–l), this work also compared the in vivo neural signal recording results of stretchable bumped electrodes and stretchable planar electrodes with the same structural design. From the comparison results, the influence of the bumped electrode structures on the SNR is significant; it is much higher than that of the flat one. From the perspective of contact impedance, although the difference between the planar electrode and the bumped electrode is not significant, the impedance deviation between different electrode sites of the planar electrode is relatively large. This indicates that the contact effect between the planar electrodes and the surface of the dura mater is inferior to that of the bumped electrodes. Furthermore, from the perspective of power density spectrum, the signal power of the bumped electrode is significantly higher than that of the planar electrode throughout the entire frequency range. This further demonstrates that the bumped electrodes are more closely adhered to the surface of the dura mater, resulting in less power attenuation of the signal. This might be the main reason why the bumped ECoG electrodes have a higher SNR.

Chronic neural signals recording and optical stimulation

In the acute implantation experiment, no dental cement was used to isolate the skull from the interior of the chamber. Additionally, the electrode connector lacked adequate protection, allowing tissue-derived water vapor to seep into the connector—this led to short circuits between channels. As a consequence, the electrode essentially lost its recording capability after ~2 weeks. Furthermore, only four bone screws were employed to secure the chamber, which resulted in the chamber becoming detached during subsequent impact events. To address these issues, the following improvements (Fig. 7(a–d)) were implemented to the chamber design and its fixation method: The square chamber was reconfigured into an elliptical shape (matching the anatomical structure of the skull), with a corresponding increase in internal volume. The number of fixing lugs (for securing the chamber to the skull) was increased from four to eight. A rubber gasket was added between the



chamber body and its lid to prevent water ingress during the rearing period. Dental cement was used to fully encapsulate the skull within the chamber, thereby

blocking bodily fluids from entering the chamber interior. Waterproof tape was applied to protect the connection points, preventing water vapor from penetrating them.

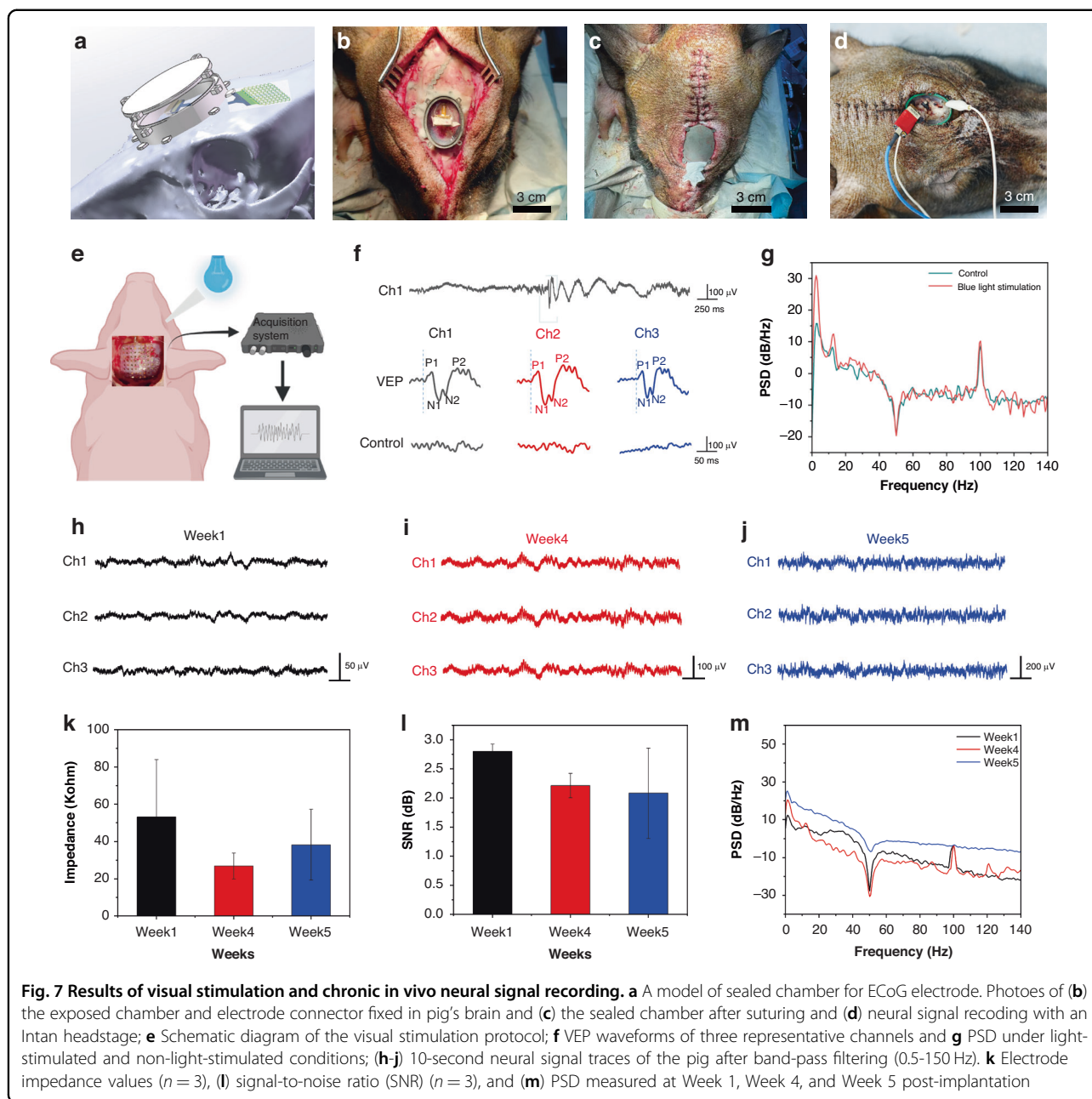


Fig. 7 Results of visual stimulation and chronic in vivo neural signal recording. **a** A model of sealed chamber for ECoG electrode. Photos of **(b)** the exposed chamber and electrode connector fixed in pig’s brain and **(c)** the sealed chamber after suturing and **(d)** neural signal recording with an Intan headstage; **e** Schematic diagram of the visual stimulation protocol; **f** VEP waveforms of three representative channels and **g** PSD under light-stimulated and non-light-stimulated conditions; **(h–j)** 10-second neural signal traces of the pig after band-pass filtering (0.5–150 Hz). **k** Electrode impedance values ($n = 3$), **(l)** signal-to-noise ratio (SNR) ($n = 3$), and **(m)** PSD measured at Week 1, Week 4, and Week 5 post-implantation

To verify the functionality of the electrode, a blue LED array (as shown in Fig. 7e) was used to stimulate the pig’s retina, thereby evoking neural activity in the visual cortex and enabling simultaneous recording. Figure 7f displays the visual evoked potential (VEP) waveforms of three representative channels under both light-stimulated and non-light-stimulated conditions in the 4th week. It is evident that at the exact moment the light stimulation is turned on, a distinct fluctuation appears in the ECoG signals. Upon magnification of this fluctuation, its waveform is found to contain two positive peaks (P1, P2) and two negative peaks (N1, N2)—these characteristic peaks

are typical markers of VEP. In contrast, when no light stimulation is applied, the ECoG signal shows no significant fluctuation, indicating the absence of VEP. Figure 7g compares the changes in the ECoG signal’s power spectrum before and after light stimulation, it can be observed that retinal stimulation by light leads to a power peak caused by low-frequency neural activity, which is precisely attributed to the VEP.

Judging from the waveform changes of the neural signals recorded in Fig. 7(h–j), the overall amplitude of the ECoG signals showed a significant increase in the 4th and 5th weeks. At the same time, as can be seen from

Fig. 7(k, l), the interfacial impedance of the electrode increased significantly, and the signal-to-noise ratio (SNR) of the recorded neural signals decreased significantly in the 4th and 5th weeks. This is because the increase in impedance raised the amplitude of the noise baseline, resulting in a decrease in the SNR from 2.6 dB in the first week to 2.1 dB in the fifth week. From the power spectrum in Fig. 7m, it can be seen that the amplitude variation of the ECoG signal in the fourth week is mainly due to the enhancement of the power of signals below 10 Hz. This low-frequency signal fluctuation may be attributed to the shallow anesthetic depth of the swine, which caused relatively obvious motion artifacts. And in the fifth week, the amplitude increase of the ECoG signal was observed throughout the entire low-frequency range. The PSD changes of neural signals may be related to the depth of anesthesia, motion artifacts, and environmental interference. They show no direct correlation with the impedance or SNR. Overall, the stretchable bumped ECoG electrodes and their implantation method proposed in this study can enable long-term and stable neural signal recording in large animals. Their interface contact performance and neural signal recording performance are significantly superior to those of stretchable or non-stretchable planar counterparts.

Discussion

In this work, limited by the height and shape of the bumped electrode points, this ECoG electrode cannot penetrate into the brain tissue to collect more abundant neural activity. Its bumped SU-8 structure has a relatively large diameter and a relatively low height, making it difficult to form an ideal microneedle structure through under-exposure. The preparation of microneedles must comply with the diffraction regulation principle based on backside exposure lithography, and the shape of microneedles is affected by the aperture of the photomask and the contact spacing. When the conditions of large aperture and short spacing are met, the system exhibits Fresnel near-field diffraction, and the ultraviolet light forms a Bessel function-type light intensity distribution. In this case, a cylindrical structure is formed after SU-8 exposure. When the conditions of small aperture and long spacing are satisfied, Fraunhofer far-field diffraction occurs, and the ultraviolet light presents a Gaussian-type light intensity distribution. At this time, a steep microneedle structure is formed after SU-8 exposure. When the parameters are in a critical state, the near-field and far-field diffractions produce a nonlinear coupling effect, and their superimposed light field can form a smooth intensity gradient, which is the key mechanism for constructing ideal microneedles. Therefore, future work may consider reducing the aperture of the microneedle pattern on the photomask and appropriately increasing the spacing

between the photomask and the substrate to optimize the microneedle structure. In addition, another advantage of the bumped electrode points is their large contact area, which endows them with high charge injection capability. This also enables them to exhibit excellent electrical stimulation performance, making them potentially applicable for visual cortex stimulation. Thus, conducting research on microneedle electrode and the modification materials for long-term electrical stimulation is also a key research direction.

Conclusion

In this work, a stretchable ECoG electrode with bumped electrodes array was developed for high conformal neural recording. This new type of structural design enables the electrodes to possess excellent electrochemical stability, tensile stability and adhesion stability simultaneously. In vitro experiments showed that the electrochemical impedance of the PEDOT modified electrode at 1 kHz remain almost constant after 4000 cycles of CV scanning and increased only 4.4% after 2500 cycles of 10% stretching, which indicates the electrode's excellent electrochemical and stretchability stability. The simulated neural recording experiments showed the PEDOT-modified stretchable electrode has the optimal ability to record the simulated neural signals, mainly due to its lower interface impedance and tighter interface adhesion ability. The in vivo recording experiments in swine's brains have shown that this stretchable electrode can stably record neural signals and maintain a high SNR and a low interface impedance after five weeks of implantation. The research indicates that this new type of electrode structure is of great significance for low-noise and high-conformal neural recording applications.

Materials and methods

Electrochemical modification

To improve electrochemical properties and reduce noises of the electrode, the gold electrode sites were modified with PEDOT/PPS layer. First, 500 mg of Sodium Polystyrenesulfonate (PSSNa) was weighed and dissolved completely in deionized water, then diluted to a final volume of 100 mL. After that, 100 μ L of Ethylenedioxythiophene (EDOT) was added and stirred with a magnetic stirrer for over 2 h. PEDOT/PSS was electrodeposited onto the electrode sites by applying a current pulse (current density of 1 mA/cm²) for a duration of 600 s. The current pulses are generated by an electrochemical workstation (CHI660E, CH instrument) with a Pt wire as counter electrode. The electrochemical impedance spectra (EIS) are measured in phosphate buffered saline (PBS, 0.1 M, pH 7.4) with saturated calomel electrode (SCE) as reference electrode and a Pt foil as counter electrode. The EIS is measured at a frequency

range from 0.1 Hz to 100,000 Hz with input voltage amplitude of 0.01 V. The scanning voltage range of the Cyclic Voltammetry (CV) curve is -0.6 V to 0.8 V, and the scanning rate is 0.1 V/s.

Photoelectric signal measurement

The photoelectric signals testing system consisting of a blue laser diode (473 nm), an electrochemical workstation (CHI660E, CH instrument) and an Evaluation System (RHD2000, Intan Technology, LA, CA). The electrochemical workstation was used to drive a laser diode (LD) to irradiate on a silicon wafer to induce photovoltaic (PV) signals in PBS to mimic neural signal as illustrated in Fig. 5(a, b). The generation of the PV signal is based on the photovoltaic effect of the silicon wafer. When light irradiates the silicon wafer, electron-hole pairs are generated. Since the mobility of electrons is higher than that of holes, electrons migrate to the surface of the silicon wafer, rendering it negatively charged. As cations in the electrolyte migrate toward the silicon wafer surface under the influence of the electrostatic field, the negative potential on the silicon wafer surface gradually decreases until equilibrium is reached. Therefore, an instantaneous negative pulse waveform is generated at the interface between the silicon wafer and the electrolyte when the light is turned on. This process is similar to the membrane potential change of neuron cells upon activation and can be used to simulate neuronal action potentials. The ECoG electrode was fixed on a micromanipulator and attached to the surface of a cerebral cortex model (a mixture of PBS and AGAR) to record the PV signals inside a shielding box. A series of blue light pulses (450 nm) with a frequency of 10 Hz, duration of 10 ms, bias current of 10 mA, and drive current of 250 mA was employed to generate the PV signals. The RHD2000 was used to record the PV signals from the ECoG electrode. The amplitude of the PV signal was defined as the “peak to peak” voltage amplitude generated during the light-on period. The signal-to-noise ratio (SNR) of the PV signal is defined as the ratio of the RMS amplitude of the PV signal to that of the background noise signal.

Mechanical properties test

Mechanical property tests mainly include the electrochemical stability, tensile stability and adhesion stability of the electrode. To test the electrochemical stability of the modification material, 4000 cycles of CV scanning from -0.6 V to 0.8 V with scanning rate of 1 V/s was conducted in PBS solution. In terms of stretchability, the electrodes with AB junctions were fixed on the stage of a mechanical testing machine (P300, Dongri Instrument) and subjected to 2500 cycles of 10% tensile strain to evaluate their mechanical durability under repeated deformation. To test the adhesion performance, the electrodes were fixed

on surface of a brain model ($5.9 \times 4.6 \times 4.2$ cm³), and then the conformality between the electrodes and the brain model was observed from different perspectives. Subsequently, the mechanical testing machine was used to test the pulling force required for the electrode to slide relative to the tangent plane of the cerebral cortex.

In vivo animal experiments

In-vivo neural recording experiments were performed on a 35 kg Bama mini pig, and all animal experiments were approved by the Zhejiang University Animal Ethics Committee. Prior to surgery, the pig was fasted for 12 h and deprived of water for 6 h. Anesthesia was induced via intravenous injection of Zoletil (10 mg/kg), and the pig was placed in a prone position within a stereotaxic frame. Anesthesia was maintained by intubation with 1.5% isoflurane, and vital signs such as heart rate and blood oxygen saturation were continuously monitored during the procedure. Surgery was performed under strict aseptic conditions. After shaving and disinfecting, the scalp was incised along the midline to expose the skull. The primary motor cortex was located according to the fontanel and sagittal suture, followed by a craniotomy using a cranial drill (78001, RWD Life Sciences, China) to remove a bone flap and the dura mater. Electrodes were placed on the cortical surface, and covered with an artificial dura. The dura and artificial dura were closed with 2-0 absorbable sutures, the bone flap was repositioned, and fixed with titanium chains and screws. Finally, a 3D-printed protective chamber was installed. Postoperatively, the pig was kept warm, injected with cephalosporin (20 mg/kg) and atropine (0.05 mg/kg), with daily wound disinfection to prevent infection. Acute ECoG signals were recorded using a CereCube system (NeuroXess, China) and chronic ECoG signals were recorded using an μ 32-channel headstage (Intan technologies, USA) at a sampling rate of 30 kHz. The titanium alloy chamber fixed on the skull is used as the reference and ground for the recording electrodes. After 1 week of implantation, ECoG signals and interface impedance were remeasured every one week. The ECoG signals were band-pass filtered between 5 and 250 Hz.

Acknowledgements

The authors thank financial support from STI 2030—Major Projects (2022ZD0208602, 2022ZD0208600), “Pioneer” and “Leading Goose” R&D Program of Zhejiang (2024C03002), Zhejiang Provincial Natural Science Foundation of China under Grant No. LQ24H180009, and National Natural Science Foundation of China (62204204).

Author details

¹MOE Engineering Research Center of Smart Microsensors and Microsystems, School of Electronics and Information, Hangzhou Dianzi University, Hangzhou, China. ²Wenzhou Institute of Hangzhou Dianzi University, Wenzhou, China. ³Center of Excellence in Biomedical Research on Advanced Integrated-on-Chips Neurotechnologies (CenBRAIN Neurotech), School of Engineering, Westlake University, Hangzhou, China. ⁴National Key Laboratory of Unmanned Aerial Vehicle Technology, Unmanned System Research Institute, School of Artificial Intelligence, Northwestern Polytechnical University, Xi’an, China.

⁵Qiushi Academy for Advanced Studies, Zhejiang University, The State Key Laboratory of Brain-Machine Intelligence, Department of Biomedical Engineering, Zhejiang University, Hangzhou, China. ⁶Department of Neurosurgery, Sir Run Run Shaw Hospital, Zhejiang University School of Medicine, Hangzhou, China

Author contributions

Designing research: M. W., H. J., C. N. Device fabrication: H. J., C. N., S. S. FEA simulation: B. J., X. Y., C. N. Data analysis: S. S., H. J., C. N., X. Y., Y. X. In vitro experiments: X. Z., C. Z., W. W., W. Z. In vivo experiments: S. Z., Y. X., L. S. Writing—original draft: C. N., H. J., M. W. Writing—review & editing: B. J., X. W., S. Z., M. W.

Data availability

The data that support the findings of this study are available from the corresponding authors upon reasonable request.

Competing interests

The authors declare no competing interests.

Ethics approval and consent to participate

This study was approved by the Zhejiang University Animal Ethics Committee, no 28423. All study methods were carried out in accordance to relevant guidelines and regulations. Verbal consent from Participants was obtained during the data Collection process as approved by the Zhejiang University Animal Ethics Committee.

Supplementary information The online version contains supplementary material available at <https://doi.org/10.1038/s41378-026-01180-w>.

Received: 14 October 2025 Revised: 20 November 2025 Accepted: 9 December 2025

Published online: 16 March 2026

References

- Maynard, E. M., Nordhausen, C. T. & Normann, R. A. The Utah intracortical electrode array: a recording structure for potential brain-computer interfaces. *Electroencephalogr. Clin. Neurophysiol.* **102**, 228–239 (1997).
- Fu, C. Y. et al. Increased risk of post-stroke epilepsy in Chinese patients with TRPM6 polymorphism. *Neurol. Res.* **41**, 378–383 (2019).
- Du, Z. J. et al. Ultrasoft microwire neural electrodes improve chronic tissue integration. *Acta Biomater.* **53**, 46–58 (2017).
- Cao, H. et al. An integrated μ LED optrode for optogenetic stimulation and electrical recording. *IEEE Trans. Biomed. Eng.* **60**, 225–229 (2012).
- Kim, T. et al. Injectable, cellular-scale optoelectronics with applications for wireless optogenetics. *Science* **340**, 211–216 (2013).
- Reddy, J. W. et al. High density, double-sided, flexible optoelectronic neural probes with embedded μ LEDs. *Front. Neurosci.* **13**, 745 (2019).
- Tchoe, Y. et al. Human brain mapping with multithousand-channel PtNRGrids resolves spatiotemporal dynamics. *Sci. Transl. Med.* **14**, eabj1441 (2022).
- Konrad, P. E. et al. First-in-human experience performing high-resolution cortical mapping using a novel microelectrode array containing 1,024 electrodes. *J. Neural Eng.* **22**, 026009 (2025).
- Sohal, H. S. et al. The sinusoidal probe: a new approach to improve electrode longevity. *Front. Neuroeng.* **7**, 10 (2014).
- Ji, B. et al. Stretchable parylene-C electrodes enabled by serpentine structures on arbitrary elastomers by silicone rubber adhesive. *J. Materiom.* **6**, 330–3389 (2020).
- Jung, H. H. et al. Highly deformable double-sided neural probe with all-in-one electrode system for real-time in vivo detection of dopamine for Parkinson's Disease. *Adv. Funct. Mater.* **34**, 2311436 (2024).
- Lee, S. et al. Stretchable surface electrode arrays using an alginate/PEDOT:PSS-based conductive hydrogel for conformal brain interfacing. *Polymers* **15**, 1 (2023).
- Baek, D. H. et al. A thin film polyimide mesh microelectrode for chronic epidural electrocorticography recording with enhanced contactability. *J. Neural Eng.* **11**, 046023 (2014).
- Ji, B. et al. Flexible and stretchable opto-electric neural interface for low-noise electrocorticogram recordings and neuromodulation in vivo. *Biosens. Bioelectron.* **153**, 112009 (2020).
- Zhao, S. et al. Tracking neural activity from the same cells during the entire adult life of mice. *Nat. Neurosci.* **26**, 696–710 (2023).
- Ji, B. et al. Brainmask: an ultrasoft and moist micro-electrocorticography electrode for accurate positioning and long-lasting recordings. *Microsyst. Nanoeng.* **9**, 126–139 (2023).
- Qi, D. et al. Highly stretchable, compliant, polymeric microelectrode arrays for in vivo electrophysiological interfacing. *Adv. Mater.* **29**, 1702800.1–1702800.10 (2017).
- Zhang, J. et al. Stretchable transparent electrode arrays for simultaneous electrical and optical interrogation of neural circuits in vivo. *Nano Lett.* **18**, 5142–5148 (2018).
- Tybrandt, K. et al. High-density stretchable electrode grids for chronic neural recording. *Adv. Mater.* **30**, e1706520 (2018).
- Chu, S. S. et al. Development of highly sensitive, flexible dual L-glutamate and GABA microsensors for in vivo brain sensing. *Biosens. Bioelectron.* **222**, 114941 (2023).
- Wurth, S. et al. Long-term usability and bio-integration of polyimide-based intra-neural stimulating electrodes. *Biomater* **122**, 114–129 (2017).
- Malekshoaraie, M. H. et al. Fully flexible implantable neural probes for electrophysiology recording and controlled neurochemical modulation. *Microsyst. Nanoeng.* **10**, 91 (2024).
- Dong, R. H. et al. Stretchable, self-rolled, microfluidic electronics enable conformable neural interfaces of brain and vagus neuromodulation. *ACS Nano* **18**, 1702–1713 (2024).
- Yang, D. et al. Double-microcrack coupling stretchable neural electrode for electrophysiological communication. *Adv. Funct. Mater.* **33**, 2300412 (2023).
- Qi, D. P. et al. Highly stretchable gold nanobelts with sinusoidal structures for recording electrocorticograms. *Adv. Mater.* **27**, 3145–3151 (2015).
- Oribe, S., Yoshida, S., Kusama, S., Osawa, S. I. & Nishizawa, M. Hydrogel-based organic subdural electrode with high conformability to brain surface. *Sci. Rep.* **9**, 14634 (2019).
- Jiang, Y. et al. Topological supramolecular network enabled highly conductive and stretchable organic bioelectronics. *Science* **378**, 1461–1467 (2022).
- Momin, M. et al. 3D-printed flexible neural probes for recordings at single-neuron level. *Device* **2**, 100519 (2024).
- Kwon, K. Y., Weber, A. & Li, W. Varying-length polymer microneedle arrays fabricated by droplet backside exposure. *J. Microelectromech. Syst.* **23**, 1272–1280 (2014).
- Qinai, Z. et al. Highly stretchable and customizable microneedle electrode arrays for intramuscular electromyography. *Sci. Adv.* **10**, eadh2230 (2024).
- Wang, M. et al. Direct electrodeposition of Graphene enhanced conductive polymer on microelectrode for biosensing application. *Biosens. Bioelectron.* **99**, 99–107 (2017).